Anisotropic Spin-Orbit Torque through Crystal-Orientation Engineering in Epitaxial Pt

Ryan Thompson,[1] Jeongchun Ryu,[2,*] Gaeun Choi,[2] Shutaro Karube,[1,3] Makoto Kohda,[1,3,4] Junsaku Nitta,[1,3,4,†] and Byong-Guk Park[2]

[1] *Department of Materials Science, Graduate School of Engineering, Tohoku University, Sendai 980-8579, Japan*
[2] *Department of Materials Science and Engineering, KAIST, Daejeon 34141, Republic of Korea*
[3] *Center for Spintronics Research Network, Tohoku University, Sendai 980-8577, Japan*
[4] *Center for Science and Innovation in Spintronics (Core Research Cluster) Organization for Advanced Studies, Tohoku University, Sendai 980-8577, Japan*

(Received 1 September 2020; revised 3 December 2020; accepted 22 December 2020; published 28 January 2021)

One of the main objectives of spintronics is to provide power-efficient switching of magnetic layers through electrical means, and in order to achieve this goal, alternate material systems with enhanced spin-orbit torque (SOT) must be engineered. In this work we provide evidence of anisotropy in the SOT and spin Hall effect (SHE) in epitaxial Pt(110) grown on MgO(110) single-crystal substrates, and find that the spin Hall angle and the dampinglike torque are 20% larger when current is applied along the [001] crystallographic direction as compared to [1$\bar{1}$0], leading to an equivalent reduction in switching current density along [001]. The anisotropy in SOT is attributed to the bulk contributions of the SHE in the Pt layer through its anisotropic resistance in this specific orientation. Measurements additionally suggest that the Rashba-Edelstein effect at the Pt/Ti interface due to the Pt(110) surface has a non-negligible effect on the spin diffusion length and SOT. By providing experimental evidence of the crystal orientation dependence of SOT-induced magnetization switching, this work helps to establish a path for energy-efficient magnetization switching through the alignment of devices with crystallographic directions of enhanced SOT generation.

DOI: 10.1103/PhysRevApplied.15.014055

I. INTRODUCTION

Spin-orbit torque (SOT) provides an energy efficient and electrically stable method of magnetization switching [1–4], arising from the bulk spin Hall effect (SHE) [5,6] and the interfacial Rashba-Edelstein effect (REE) [7–9] in heavy metal (HM) and ferromagnetic (FM) heterostructures. Recently, one avenue of study for enhancing spin-orbit torque has been through epitaxial growth [10–14]. One study has shown enhanced spin current generation in epitaxial Ta/(Co, Fe)B [15], and another found current-induced magnetization switching at extremely low current densities in epitaxial Au/Fe_4N [16]. In Pt, the crystalline structure has been shown to be important in determining the spin relaxation mechanism [17], and the spin-orbit field susceptibility has been calculated to be highly anisotropic in the Pt(111) surface [18]. This naturally leads to the question of how the spin current generated in such heterostructures is affected by crystallographic orientation.

The anomalous Hall effect (AHE) is inherently anisotropic, as it depends on the orientation of the magnetization M. However, while the SHE has similar origins to the AHE [19], it occurs in materials without net magnetization, so its anisotropy is less straightforward. In fact, in cubic materials, the spin Hall conductivity (SHC) is expected to be isotropic due to symmetry [20]. However, in noncubic materials the SHC can be quite anisotropic, as shown from first principals in certain hexagonal close-packed [21]. Apart from metals, anisotropic spin polarization has been observed in (Al, Ga)As quantum wells due to the wavevector **k** dependence of the Dresselhaus field [22], the epitaxial triangular antiferromagnet $IrMn_3$ has shown facet-dependent SHC [23], and anisotropic spin Hall angles were engineered by tailoring the crystalline symmetry in epitaxial $SrIO_3$ [24].

In heavy metals, however, experimental evidence of anisotropy in the SHE is lacking. One study concerning epitaxial Fe/Pt bilayers grown on MgO(001) found the spin Hall angle to be isotropic [25]. In our previous work we found strongly anisotropic spin Hall magnetoresistance (SMR) in epitaxial Pt/Co bilayers grown on MgO(110) [26], but this was found to be primarily due to the epitaxial

*jcryu@kaist.ac.kr
†nitta@material.tohoku.ac.jp

 © 2021 American Physical Society

Pt/Co interface, which caused very different spin diffusion lengths when current was applied along the [001] or [1$\bar{1}$0] direction.

In this work, we quantify the anisotropy in the SHE in epitaxial Pt(110) and provide experimental evidence of the crystal orientation dependence of SOT-induced switching by using Pt/Ti/(Co, Fe)B structures with a perpendicularly magnetized FM layer. The Ti spacer helps to provide perpendicular magnetization anisotropy as well as separating the HM and FM layers to reduce the large interfacial contributions seen previously [26]. We report a 20% enhancement in the spin Hall angle and dampinglike spin-orbit torque in the epitaxial Pt(110) when current is applied in the [001] direction as compared to the [1$\bar{1}$0] direction, measured using SMR and harmonic Hall measurements, respectively. This is further corroborated through current-induced magnetization switching experiments, in which there is a reduction in critical switching current corresponding to the increase in spin Hall angle for [001]. These findings show a particular crystallographic orientation dependence of the spin Hall effect and associated spin-orbit torque, and could provide a route for efficient magnetization switching that can be used in conjunction with other techniques such as interfacial engineering [27] or HM1/FM/HM2 sandwiches where HM1 and HM2 have opposite spin Hall angle signs [28] to further enhance SOT.

II. SAMPLE DESCRIPTION AND CHARACTERIZATION

Pt(t_N nm)/Ti(0.8 nm)/(Co, Fe)B(1 nm)/MgO(3 nm) heterostructures are sputter deposited on single-crystal MgO(110)-oriented substrates in an ultrahigh vacuum chamber, below 2×10^{-7} Pa. The Pt layer is grown at a substrate temperature of 200 °C in order to promote epitaxial growth, while the remaining layers are all grown at room temperature by allowing the samples to cool within the vacuum system. The (Co, Fe)B target had a composition of Co:Fe:B of 20%:60%:20%. The (Co, Fe)B layer is capped with MgO in order to promote perpendicular magnetic anisotropy (PMA), and the MgO layer is capped with 2 nm of Pt to prevent water absorption from the atmosphere into the MgO layer. Pt is grown at various thicknesses by adjusting the sputtering time, while the Ti layer is always 0.8 nm and the (Co, Fe)B layer is always 1 nm. Finally, the samples are postannealed at 200 °C for 40 min to induce PMA in the (Co, Fe)B, before being removed from the vacuum chamber. Hall crosses having arms with a width of 5 μm and a length of 15 μm are patterned using photolithography and Ar-ion milling, and Al metal electrical contacts are sputter deposited after fabricating the Hall crosses.

The Pt crystal structure is confirmed using in-plane XRD, as seen in Fig. 1(a). The ϕ scan shows the twofold symmetry of the (002) and (2$\bar{2}$0) peaks of Pt, overlapping the corresponding MgO substrate peaks. Out-of-plane XRD further confirms epitaxy; the MgO(110)//Pt(10 nm)/Ti(0.8 nm)/(Co, Fe)B(1 nm)/MgO(3 nm) peaks can be seen in Fig. 1(c).

In this work, the X direction is defined as the applied current J_C direction, and the Z direction is the out-of-plane direction. Note that the X and Y axes are rotated 90° when comparing the [001] and [1$\bar{1}$0] directions due to this definition. A diagram of the crystal structure of the MgO substrate and the epitaxial Pt layer can be seen in Figs. 1(d) and 1(e). The Z axis is along

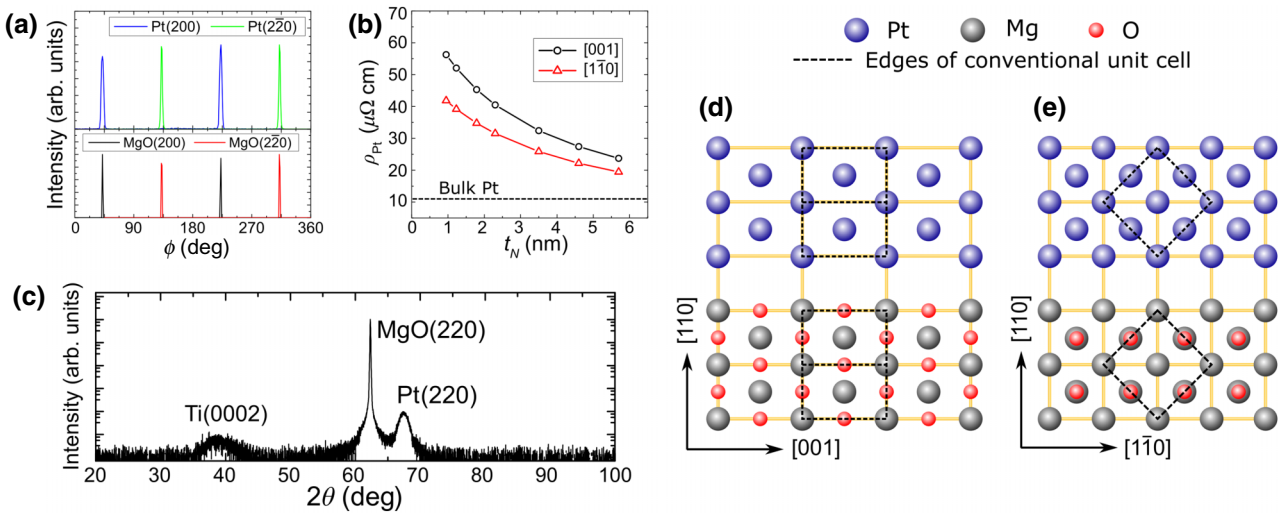

FIG. 1. (a) In plane ϕ scan showing twofold symmetry of epitaxial Pt (200) and (2$\bar{2}$0) peaks, aligned with corresponding MgO substrate peaks. (b) Extracted Pt resistivities for the [001] and [1$\bar{1}$0] directions. (c) Out of plane 2θ scan of MgO(110)//Pt(10)/Ti(0.8)/(Co, Fe)B(1)/MgO(3) sample. (d) Diagram of the (1$\bar{1}$0) plane of MgO and Pt layers. (e) Diagram of the (001) plane of MgO and Pt layers.

[110]. The conventional face-centered cubic unit cell (marked by the dashed line) is tilted 45°, so in this orientation, it is convenient to represent the unit cell as pseudotetragonal instead (marked by the orange connections), and explains the twofold symmetry seen in the ϕ scan.

The Pt resistivity ρ_{Pt} is measured to be anisotropic between the two in-plane directions, as seen in Fig. 1(b), as well as Pt thickness dependent. At all measured thicknesses, [001] is found to have higher resistivity, and the anisotropy between the two directions increases at lower Pt thicknesses. At $t_N = 1$ nm, $\rho_{\mathrm{Pt}}^{[001]}$ is about 34% larger than $\rho_{\mathrm{Pt}}^{[1\bar{1}0]}$, and only about 22% larger at $t_N = 6$ nm, as both directions approach the bulk value as the thickness increases.

III. RESULTS AND DISCUSSION

A. SMR measurements

Magnetoresistance measurements are performed using the resistivity option in a quantum design physical property measurement system for various Pt thicknesses with current applied along both the [001] and [1$\bar{1}$0] directions. Here, we define spin Hall magnetoresistance as $\Delta R_{xx}^{\mathrm{SMR}} = R_{xx}(H_Y) - R_{xx}(H_Z)$. Field scans are performed in the Pt thickness range of 1 to 6 nm, and example field scans can be seen in Fig. 2(a). All field scans are performed at 300 K. Because these samples are perpendicularly magnetized, no variation in the resistance is seen in the Z scans, while resistance decreases as a field is applied in the $\pm Y$ direction due to the combination of spin Hall and inverse spin Hall effects [29] [see Fig. 2(b) for a sample diagram].

The Pt thickness-dependent SMR results are fit using the following equation, with the assumptions of zero longitudinal spin absorption and a transparent HM/FM interface [29,30]:

$$\frac{\Delta R_{xx}^{\mathrm{SMR}}}{R_{xx}^{0}} = -\theta_{\mathrm{SH}}^{2}\frac{\lambda_{\mathrm{sf}}}{t_N}\frac{\tanh(\tau)}{1+\eta}\left[1-\frac{1}{\cosh(2\tau)}\right]. \quad (1)$$

Here θ_{SH} is the spin Hall angle, λ_{sf} is the spin diffusion length, $\eta = (\rho_N t_{\mathrm{Ti}})/(\rho_{\mathrm{Ti}} t_N)$ is the current shunting coefficient, and $\tau = t_N/2\lambda_{\mathrm{sf}}$. Since there is a large variation in ρ_{Pt}, an arbitrary equation is fit to Fig. 1(b) and substituted in for ρ_{Pt} in the current shunting coefficient, to more accurately calculate the current shunting at each thickness. Furthermore, the current is assumed to only be shunted into the Ti layer, for which we extract a resistivity of 42.8 $\mu\Omega$ cm. The resistivity of (Co, Fe)B is high enough, generally around 160 $\mu\Omega$ cm [31], that we can assume

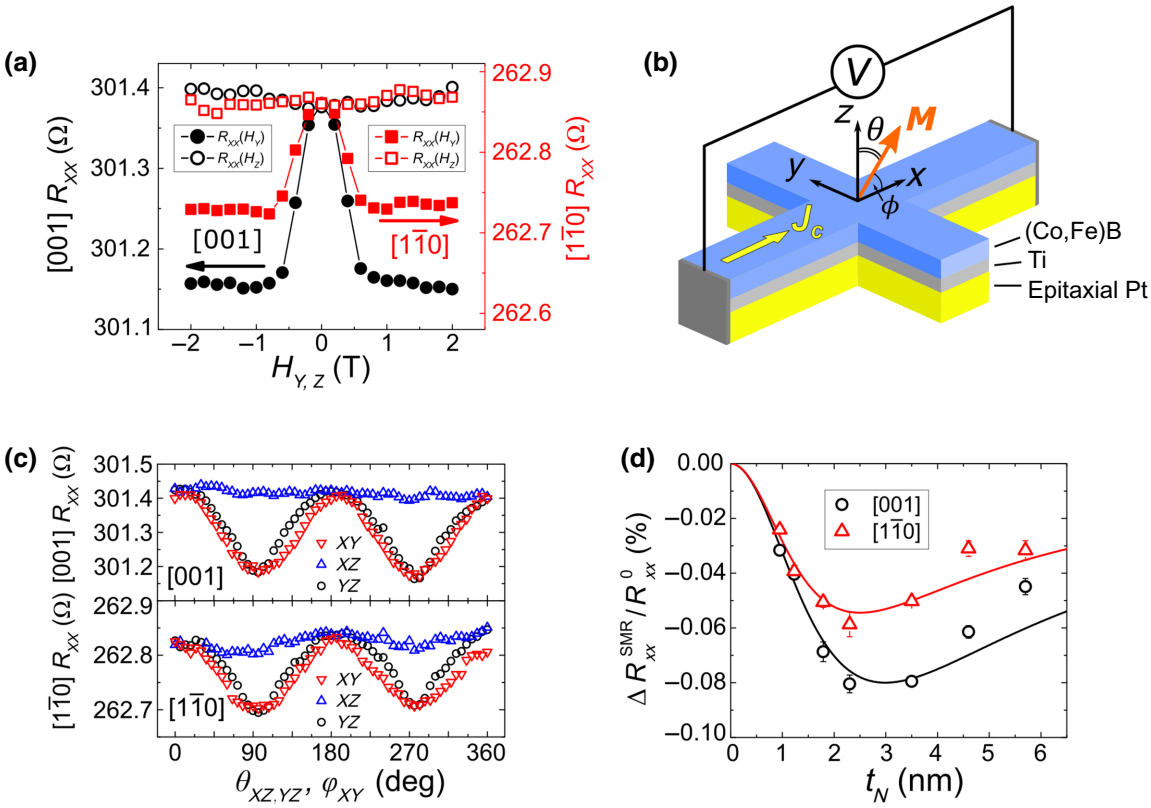

FIG. 2. (a) Example H_Y and H_Z field scans for the [001] and [1$\bar{1}$0] directions for the $t_N = 3.5$ nm sample. (b) Schematic of the Hall bar used in this measurement and the axes defined for this work. (c) Example XY, XZ, and YZ angle scans for the [001] and [1$\bar{1}$0] directions performed at 1.5 T for the $t_N = 3.5$ nm sample. (d) SMR as a function of Pt thickness fit using Eq. (1).

no current is flowing through the (Co, Fe)B layer. This assumption is supported by the negligible amplitude of the *XZ* angle scans seen in Fig. 2(c), which corresponds to the anisotropic magnetoresistance in the FM layer.

We find that the spin Hall magnetoresistance shows a significant increase in magnitude when current is applied along [001] as opposed to $[1\bar{1}0]$, as seen in Fig. 2(d). This can be attributed to the increased $\theta_{\mathrm{SH}}^{[001]} = 0.053$, approximately 20% larger than $\theta_{\mathrm{SH}}^{[1\bar{1}0]} = 0.044$. Assuming that the Elliot-Yafet (EY) spin relaxation mechanism [32,33] is dominant, the theoretical intrinsic contribution of the spin Hall angle can be calculated as $\theta_{\mathrm{SH}}^{\mathrm{int}} = \sigma_{\mathrm{SH}}^{\mathrm{int}}\rho_{\mathrm{Pt}}$. Using an intrinsic spin Hall conductivity ($\sigma_{\mathrm{SH}}^{\mathrm{int}}$) of 1600 $\Omega^{-1}\,\mathrm{cm}^{-1}$ [34] and the average conductivity for the measured thickness range, we find good agreement with $\theta_{\mathrm{SH}}^{[001],\mathrm{int}} = 0.058$ and $\theta_{\mathrm{SH}}^{[1\bar{1}0],\mathrm{int}} = 0.046$. We also find the spin diffusion length is slightly longer along [001] at $\lambda_{\mathrm{sf}}^{[001]} = 1.28$ nm than along $[1\bar{1}0]$ with $\lambda_{\mathrm{sf}}^{[1\bar{1}0]} = 1.07$ nm. The possible extent of anisotropy in λ_{sf} is discussed in Appendix A. A summary of extracted parameters can be seen in Table I.

Since λ_{sf} does not follow the directly proportional relationship with ρ_{Pt} as expected from the EY mechanism, we must consider influence from the REE that affects the spin diffusion length through the D'yakonov-Perel (DP) spin relaxation mechanism [5]. The REE has also been shown to have the same *YZ* angular dependence on magnetoresistance as SMR, known as Rashba-Edelstein magnetoresistance (REMR) [35]. In this case, the calculated spin Hall angle is likely slightly overestimated here; however, the majority of the *YZ* MR signal should be due to SMR, as we observe a large dependence on the thickness of Pt, while REMR should be independent of the Pt thickness [36].

These results are quite different from the SMR signal seen in the epitaxial MgO(110)/Pt/Co layers in Ref. [26]. In that work, current applied along $[1\bar{1}0]$ had a SMR peak at about 0.75 nm, while [001] had a peak at around 2 nm. The anisotropy in the SMR was due to $\lambda_{\mathrm{sf}}^{[001]}$ being 3 times larger than $\lambda_{\mathrm{sf}}^{[1\bar{1}0]}$, owing to the epitaxial Pt/Co interface generating a sizeable and anisotropic REE. The spin Hall angle was found to be approximately isotropic; however, the SMR model likely was not completely valid for that system. In this work, we observe different behavior: the SMR peak appears at about 2.5–3 nm, $\lambda_{\mathrm{sf}}^{[001]}$ is only about 1.2 times longer than $\lambda_{\mathrm{sf}}^{[1\bar{1}0]}$, and we find an increase in $\theta_{\mathrm{SH}}^{[001]}$. These results suggest that the EY mechanism is dominant for the MR and is the primary contribution to the spin Hall angle, while the contribution from the interfacial REE is much smaller in this work than in the Pt/Co case, allowing for the bulk contributions to be more clearly observed.

B. Harmonic Hall measurements

Harmonic Hall measurements are performed using the lock-in technique [37,38], by applying an ac current with a Keithley 6221 current source at a constant amplitude at a frequency of 19 Hz and measuring the first harmonic ($V_{xy}^{1\omega}$) and the 90° out-of-phase second harmonic ($V_{xy}^{2\omega}$) simultaneously using two SR830 lock-in amplifiers. The sample is positioned with a slight out-of-plane tilt ($\theta \sim 85°$) to prevent multidomain formation. A field is swept parallel to (H_X) or transverse to (H_Y) the current, giving the transverse and longitudinal current-induced effective fields. The experimental geometry for this measurement can be seen in Fig. 3(a), and example first and second harmonics can be seen in Figs. 3(b)–3(d).

In this geometry with samples having PMA, the first harmonic gives an anomalous Hall signal, which can be fit at low fields with a quadratic equation, while the second harmonics give linear signals at low fields that describe the magnetization oscillation due to the spin-orbit torque. The thermal contributions from the anomalous Nernst effect in the second harmonic are subtracted [39]. With a parallel field H_X applied, the dampinglike effective field (H_{DL}) is generated by the dampinglike spin-orbit torque (DLT). With a transverse field H_Y applied, the fieldlike effective field (H_{FL}) is generated by the fieldlike spin-orbit torque (FLT). We calculate the current-induced effective fields considering the non-negligible planar hall effect (PHE) using the equations [40]

$$H_{\mathrm{DL}} = \frac{B_X + 2\xi B_Y}{1 - 4\xi^2}, \qquad H_{\mathrm{FL}} = \frac{B_Y + 2\xi B_X}{1 - 4\xi^2}, \tag{2}$$

TABLE I. Extracted spin Hall angles (θ_{SH}), dampinglike effective fields per unit current ($H_{\mathrm{DL}}^{\infty}/j_{\mathrm{Pt}}$), and spin diffusion lengths (λ_{sf}) for the [001] and $[1\bar{1}0]$ directions obtained from SMR and harmonic Hall data fits. Resistivity of Pt (ρ_{Pt}) shown for the $t_N = 1$–6 nm range [seen in Fig. 1(b)].

Orientation	ρ_{Pt} ($\mu\Omega$ cm)	Measurement	θ_{SH}	$H_{\mathrm{DL}}^{\infty}/j_{\mathrm{Pt}}$ [mT/(10^{11} A/m^2)]	λ_{sf} (nm)
[001]	23.7–56.3	SMR	0.053		1.28 ± 0.04
		Harmonic Hall	0.019	0.99 ± 0.06	1.17 ± 0.13
$[1\bar{1}0]$	19.3–42.0	SMR	0.044		1.07 ± 0.04
		Harmonic Hall	0.016	0.83 ± 0.07	0.95 ± 0.16

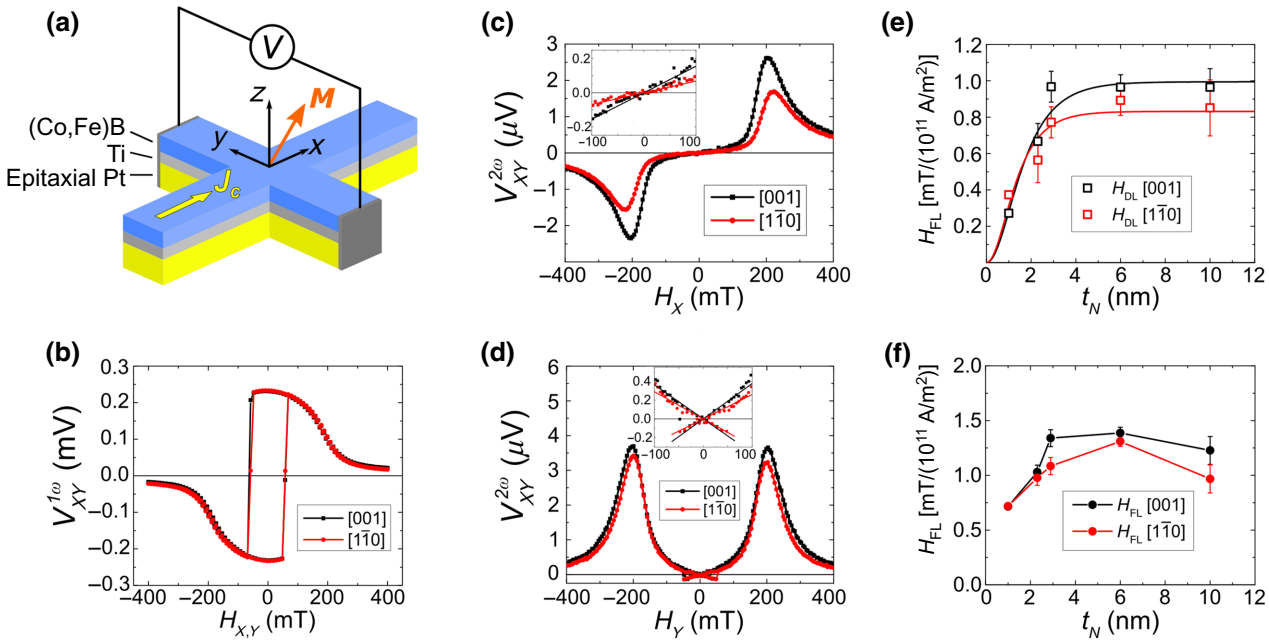

FIG. 3. (a) Schematic of the Hall bar used in this measurement and the axes defined for this work. (b) Example first harmonics of the 3 nm sample for the [001] and [1$\bar{1}$0] directions, showing no significant differences. (c) Example second harmonics of the 3 nm sample under a longitudinal field; the inset shows an enlargement of the low field. (d) Example second harmonics of the 3 nm sample under a transverse field; the inset shows an enlargement of the low field. (e) Dampinglike effective fields as a function of Pt thickness for the [001] and [1$\bar{1}$0] directions, fit using Eq. (3). (f) Fieldlike effective fields as a function of Pt thickness for the [001] and [1$\bar{1}$0] directions.

where $B_{X(Y)} = 2(\partial V_{2\omega}/\partial H_{X(Y)})/(\partial^2 V_{1\omega}/\partial H^2_{X(Y)})$ [38] and $\xi = \Delta R_P/\Delta R_A$ is the ratio of the AHE and PHE resistances (ΔR_A and ΔR_P, respectively). The AHE and PHE resistances are measured for each device [28], and we find that $\xi \approx 0.25$ for 3 nm and above samples and $\xi \approx 0.1$ for the 1 nm sample.

The effective fields per unit current in the Pt layer j_{Pt} can be seen in Figs. 3(e) and 3(f). The dampinglike effective field H_{DL} increases with Pt thickness, then saturates around 3 nm, at approximately the same Pt thickness as the peak value seen in SMR. To quantitatively compare these results to the SMR results, we fit the data using the equation [41]

$$\frac{H_{\mathrm{DL}}}{j_{\mathrm{Pt}}} = \frac{H^{\infty}_{\mathrm{DL}}}{j_{\mathrm{Pt}}}\left[1 - \mathrm{sech}\left(\frac{t_N}{\lambda_{\mathrm{sf}}}\right)\right]. \tag{3}$$

From this, we obtain $H^{\infty}_{\mathrm{DL}}/j_{\mathrm{Pt}}$ and the spin diffusion length. The obtained λ_{sf} from the effective field fitting is slightly smaller than the values obtained through the SMR fitting, with $\lambda^{[001]}_{\mathrm{sf}} = 1.17$ nm and $\lambda^{[1\bar{1}0]}_{\mathrm{sf}} = 0.95$ nm. This is likely due to an underestimation of the bulk λ_{sf} in Eq. (3) due to the nonuniformity of ρ_{Pt} [42]. Nevertheless, we find the same relation of $\lambda^{[001]}_{\mathrm{sf}} > \lambda^{[1\bar{1}0]}_{\mathrm{sf}}$ as in the SMR results.

We calculate $H^{\infty,[001]}_{\mathrm{DL}}/j_{\mathrm{Pt}} = 0.99$ mT/(10^{11}A/m^2) and $H^{\infty,[1\bar{1}0]}_{\mathrm{DL}}/j_{\mathrm{Pt}} = 0.83$ mT/(10^{11}A/m^2). This represents a 19% increase in the DLT, which is consistent with the increase in spin Hall angle calculated from SMR measurements. Note that, for this calculation, we assume all applied current is flowing through the Pt layer for simplicity, so this represents a lower bound of the effective fields. We can estimate the effective θ_{SH} from this fitting using the equation [43] (see Appendix B for details on the measurement of the saturation magnetization M_s)

$$\theta_{\mathrm{SH}} = \frac{2eM_s t_F}{\hbar}\frac{H^{\infty}_{\mathrm{DL}}}{j_{\mathrm{Pt}}}, \tag{4}$$

and find that $\theta^{[001]}_{\mathrm{SH}} = 0.019$ and $\theta^{[1\bar{1}0]}_{\mathrm{SH}} = 0.016$, qualitatively consistent with the SMR results. The fieldlike effective field H_{FL} shows the behavior of increasing with Pt thickness and then gradually decreasing for both current directions. As with H_{DL}, we find that $H^{[001]}_{\mathrm{FL}} > H^{[1\bar{1}0]}_{\mathrm{FL}}$ for all Pt thicknesses.

The Rashba-Edelstein effect contributes to both the DLT and FLT, mixing with the contributions from the SHE. While it can be difficult to disentangle, both theory [44–46] and experiment [14] have shown that the SHE contributes primarily to the DLT and that the REE contributes primarily to the FLT, meaning that the anisotropy in the DLT is unlikely to be due to the REE. Thus, we attribute the DLT signal to the bulk SHE in Pt(110), which is consistent with the SMR measurements. The anisotropy that is seen in the FLT in Figs. 3(d) and 3(f), however, can likely be attributed to the REE.

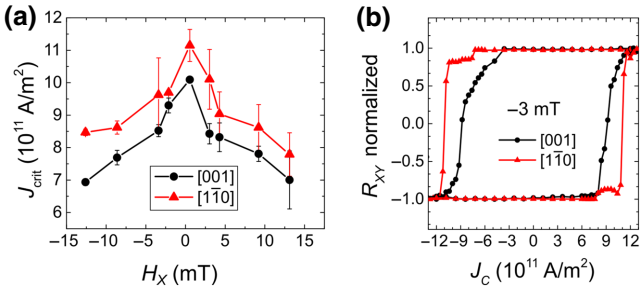

FIG. 4. (a) Critical switching current J_{crit} in the $t_N = 4.5$ nm sample as a function of applied field H_X for the [001] and [1$\bar{1}$0] directions. (b) Example loop showing reduced J_{crit} for [001] at $H_X = -3$ mT.

C. Current-induced magnetization switching

Finally, switching measurements are performed in order to directly see the effect of an increased spin Hall angle in the [001] direction. Measurements are performed in ambient conditions using the same electromagnet setup as for harmonic Hall measurements, with a Keithley 6221 as the current source applying dc current pulses J_C with a pulse width of 15 μs. A Keithley 2182a nanovoltmeter is used to measure the Hall voltage with a read current of 1 mA. The current J_C is swept along x, and the Hall voltage is measured to detect the magnetization state based on the anomalous Hall effect. In order to get deterministic switching, a field H_X is also applied along $\pm x$ [1].

At all tested fields, the [001] direction is seen to have a decreased critical switching current J_{crit}, the results of which can be seen in Fig. 4(a). Error bars in this plot represent multiple measurements and intermediate switching states, which are due to different domains having different nucleation thresholds, as these Hall bars are much larger than the size of a single domain.

$J_{crit}^{[001]}$ was reduced by an average of 18% over all tested fields, which is consistent with the 20% increase in $\theta_{SH}^{[001]}$ and the 18% increase in $H_{DL}^{[001]}$. An example loop showing the reduced J_{crit} for current applied along [001] can be seen in Fig. 4(b). An important consideration here is that, while $J_{crit}^{[001]}$ is lower, $\rho_{Pt}^{[001]}$ is larger, requiring a larger voltage to achieve the same current density. To better compare the energy consumption in a practical sense between these two directions, we calculate the threshold power $P_{sw} = J_{crit}^2 \rho_{Pt}$ for [001] and [1$\bar{1}$0]. For the measured field range, we find that $P_{sw}^{[001]}$ is reduced by about 10% on average compared to $P_{sw}^{[1\bar{1}0]}$, with both of the order of 0.1 W.

D. Discussion of anisotropy

Now that we have established the enhancement of spin current along [001], we discuss the possible origins of these results. First we consider the contributions to the total SOT, which can be described as SOT_{total} = MgO/Pt interface + Pt bulk + Pt/Ti interface + Ti bulk + Ti/(Co,Fe)B interface. However, we can reduce this to simply SOT_{total} = Pt bulk + Pt/Ti interface for the following reasons. (1) The MgO(110)/Pt interface may contribute to the REE, but since the spin diffusion length of Pt is only approximately 1 nm, this interface is too far removed from the (Co,Fe)B to have any sizeable impact. (2) Ti is a light 3d element that has very low spin-orbit coupling and a negligible spin Hall angle, so we can ignore any contributions from the Ti bulk [47]. (3) Ti/(Co,Fe)B bilayers with PMA have previously been shown to generate negligible DLT [48], and any contribution it does have should be isotropic due to the polycrystalline Ti. Hence, the contributions to the anisotropy in SOT are narrowed down to the Pt bulk and the Pt/Ti interface.

First, we examine the bulk contributions of the Pt. We calculate the intrinsic spin Hall angles for [001] and [1$\bar{1}$0] in the SMR section using an intrinsic spin Hall conductivity based on the EY mechanism in Pt, and find good agreement with the spin Hall angles extracted from our SMR measurements. The ratio of $\theta_{SH}^{[001]}$ to $\theta_{SH}^{[1\bar{1}0]}$ is approximately the same as the ratio of $H_{DL}^{[001]}$ to $H_{DL}^{[1\bar{1}0]}$, and this also corresponds to the ratio of $\rho_{Pt}^{[001]}$ to $\rho_{Pt}^{[1\bar{1}0]}$, which is expected from the EY mechanism. Lastly, we observe the Pt thickness dependence of SMR and H_{DL} expected from theory, which must be due to bulk contributions by definition. Thus, we conclude that the spin Hall angle and the DLT are dominated by bulk EY contributions.

According to the EY mechanism, the spin diffusion length is inversely proportional to the resistivity, as is normally the case in Pt [34]. However, in this work, the resistivity and spin diffusion length show that $\rho_{Pt}^{[001]} > \rho_{Pt}^{[1\bar{1}0]}$ and $\lambda_{sf}^{[001]} > \lambda_{sf}^{[1\bar{1}0]}$, which cannot be explained by the EY mechanism alone. We therefore conclude that there are contributions from both the EY and DP mechanisms, which have previously been observed in epitaxial Pt layers [17]. Based on the results of the SMR and harmonic Hall measurements, we determine that the EY mechanism is dominant in the bulk, but that the DP mechanism arises at the Pt/Ti interface due to the REE. The REE appears at heterogeneous interfaces due to the spin sub-bands becoming split in momentum, which causes a nonzero spin density to be generated [49]. Since the REE is dependent on the band structure at the interface, the symmetry of the Pt(110) surface allows an anisotropic Rashba term to appear [50] (see Appendix C), and as such, we do not expect Ti to play an important role. Larger anisotropy in λ_{sf} was observed in the epitaxial Pt(110)/epitaxial Co system [26], which shows the importance of a clean Pt(110) surface for this effect. The effective field induced by the REE causes spins to precess and lose their polarization through the DP mechanism, which could lead to the unexpected λ_{sf}/ρ_{Pt} relationship observed here. From this, we determine that modulation

of the spin diffusion length is due to the REE caused by the Pt(110) surface.

Following these considerations, both the SHE (from Pt bulk contributions) and the REE [from Pt(110)/Ti interfacial contributions] should be anisotropic with regards to the crystallographic orientation in order to adequately explain all the results presented in this work, with the bulk Pt dominating the SMR and DLT, and the interfacial REE modulating the spin diffusion length and FLT.

IV. CONCLUSION

In summary, we find that the spin Hall angle in epitaxial Pt(110) is approximately 20% larger when current flows along the [001] direction as compared to the $[1\bar{1}0]$ direction through SMR measurements. This is supported by harmonic Hall measurements where we also observe a similar enhancement in the DLT along [001]. Through consideration of the sources of SOT, we determine that this anisotropy arises due to the specific crystallographic orientation of Pt, yielding an anisotropic spin Hall effect as a consequence of the anisotropic resistivity. The spin diffusion length and FLT are further modified through an anisotropic REE at the Pt/Ti interface due to the structure of the Pt(110) surface. This work culminates in current induced magnetization switching measurements, where nearly 20% less current density is needed to switch the magnetization direction when current is applied along [001], showing a direct correlation between switching efficiency and crystallographic orientation.

The literature for spin-orbitronic epitaxial systems is still limited, so there remains much room for advancements that could be beneficial for applications. This report sheds light on the interesting crystallographic dependencies of SOTs, and helps to provide an avenue for enhancing SOT generation through alignment of devices with crystallographic axes. This effect can likely be enhanced even further, especially through specific interface engineering or higher quality interfacial growth in systems with unique orientations. These results establish another viable approach to manipulating SOT and the switching efficiency, and will inspire further research into the crystallographic orientation engineering of spin currents.

ACKNOWLEDGMENTS

R.T. is supported by the Graduate Program in Spintronics at Tohoku University. S.K., M.K., and J.N. acknowledge financial support from the Japanese Ministry of Education, Culture, Sports, Science, and Technology (MEXT) in Grant in-Aid for Scientific Research (Grant No. 15H05699), the JSPS Core-to-Core Program (Grant No. JPJSCCA20160005), and a research grant from the Tanaka Precious Metals Memorial Foundation. J.R. and B.-G.P acknowledge financial support from the National Research Foundation of Korea (Grants No. 2015M3D1A1070465 and No. 2020R1A2C2010309) and the KAIST College of Engineering Global Initiative Convergence Research Program.

APPENDIX A: SPIN DIFFUSION LENGTH ANISOTROPY

In the main text, we calculate the spin diffusion length λ_{sf} by fitting the Pt thickness-dependent SMR data, and find that $\lambda_{sf}^{[001]} = 1.28$ nm and $\lambda_{sf}^{[1\bar{1}0]} = 1.07$ nm. The peak position of SMR is primarily determined by λ_{sf} [29], so here we more closely examine the possible extent of the anisotropy in λ_{sf}.

We extend Fig. 2(b) in the main text here by adding 99% confidence bands, as indicated by the blue (for the [001] direction) and red (for the $[1\bar{1}0]$ direction) color bands in Fig. 5. For the [001] direction, there is little uncertainty in the peak position for the fitting equation, as the top and bottom of the blue band have roughly the same peak position. There is larger variance in the $[1\bar{1}0]$ direction, around 0.5 nm difference between the lower and the upper edges of the band. The upper edge of the $[1\bar{1}0]$ band is at nearly the same position as the [001] band, but the lower edge is at a much smaller thickness than for [001]. Using these 99% confidence bands, we conclude that $\lambda_{sf}^{[1\bar{1}0]} \leq \lambda_{sf}^{[001]}$, and that it is highly unlikely for $\lambda_{sf}^{[1\bar{1}0]}$ to be larger than $\lambda_{sf}^{[001]}$.

As explained in the main text, in the regime of EY being the dominant spin relaxation mechanism, resistivity ρ and λ_{sf} should be inversely proportional, but this is not the case for this system. Based on this measurement, ρ and λ_{sf} are either directly proportional, or λ_{sf} has no dependence on ρ.

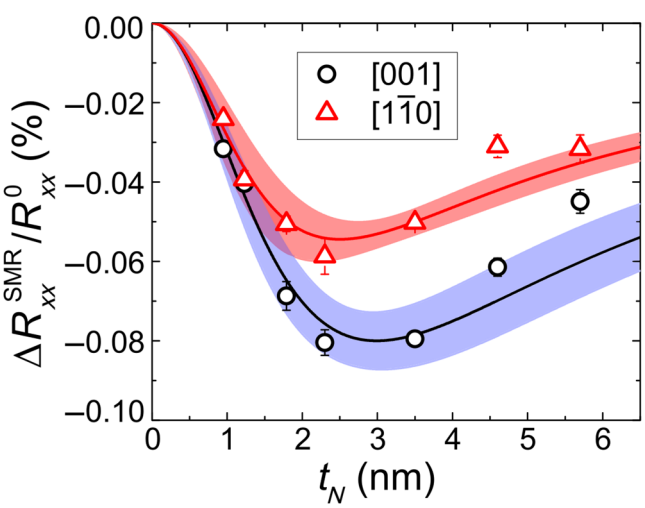

FIG. 5. SMR as a function of thickness with added 99% confidence bands of fitting.

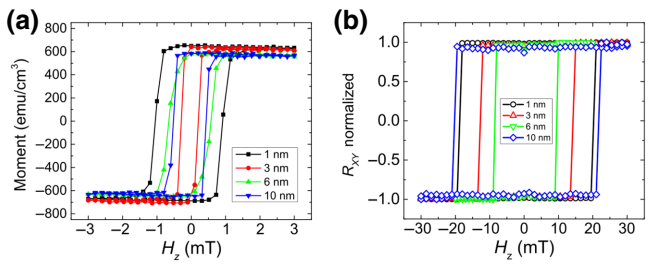

FIG. 6. (a) Hysteresis loops with an out-of-plane field H_Z of $t_N = 1$, 3, 6, and 10 nm samples as grown, measured in a VSM. (b) Normalized Hall resistances after Hall cross fabrication.

APPENDIX B: MAGNETOMETRY

The magnetic properties of the structures are measured both before and after Hall cross patterning. All samples showed PMA both before and after patterning. Before patterning, the samples are measured using a vibrating sample magnetometer (VSM) and have coercivities H_c between approximately 0.2–1 mT, depending on the sample. The samples have an average saturation magnetization M_S of 632 emu/cm^3. Example out-of-plane hysteresis loops measured in the VSM can be seen in Fig. 6(a).

After patterning, the samples are measured using the anomalous Hall effect, and H_c is found to have increased to between approximately 5–30 mT, depending on the device. Different devices show different coercivities, and there is no direct dependence on coercivity with the Pt thickness. Coercivity likely increased for patterned devices due to the smaller surface area of the (Co,Fe)B, leading to a lower probability of an easily switchable magnetic domain. A few example Hall resistances can be seen in Fig. 6(b). The Hall resistances are normalized to show all in one figure because the magnitude of the Hall resistance is inversely proportional to the Pt thickness, due to current shunting out of the (Co,Fe)B layer.

APPENDIX C: ANISOTROPY IN THE REE

We propose two possible origins for the anisotropy in the REE. First, in this (110) orientation, there is a direction with larger atomic spacing and a direction with shorter atomic spacing, as shown in Figs. 1(d) and 1(e) in the main text, so this could contribute to a difference in charge distribution at the Pt/Ti interface along these two directions, giving rise to an anisotropic REE. The strength of the Rashba spin-orbit coupling is defined by the Rashba parameter α_R, and can be defined as [50]

$$\alpha_R = \frac{\hbar^2}{4m^2c^2} \int d^3r\, \partial_z V(\mathbf{r})\, |\psi(z)|^2 , \qquad \text{(C1)}$$

where m is the mass of the electron, c is the speed of light, $\partial_z V(\mathbf{r})$ is the crystal potential gradient perpendicular to the interface, and $|\psi(z)|^2$ is the electron density distribution. While $|\psi(z)|^2$ is generally localized within 1 bohr of the HM atomic nucleus [51], the precise form and asymmetry of $|\psi(z)|^2$ is also determined by the surface potential [52], which could be asymmetric in plane in the current work, leading to an anisotropic α_R.

Second, because the Rashba Hamiltonian represents a momentum-dependent split in the spin sub-bands, the REE can become direction dependent if the effective mass m^* as determined by the band structure is also direction dependent, as was calculated for monolayer black phosphorous [53]. For the case of the Pt(110) surface, which has the reduced symmetry of the C_{2v} point group, *ab initio* calculations predict such anisotropic Rashba splitting (and consequently α_R) for this point group as well [50].

[1] I. M. Miron, K. Garello, G. Gaudin, P.-J. Zermatten, M. V. Costache, S. Auffret, S. Bandiera, B. Rodmacq, A. Schuhl, and P. Gambardella, Perpendicular switching of a single ferromagnetic layer induced by in-plane current injection, Nature **476**, 189 (2011).

[2] L. Liu, C.-F. Pai, Y. Li, H. W. Tseng, D. C. Ralph, and R. A. Buhrman, Spin-torque switching with the giant Spin Hall effect of tantalum, Science **336**, 555 (2012).

[3] A. Manchon, J. Železný, I. M. Miron, T. Jungwirth, J. Sinova, A. Thiaville, K. Garello, and P. Gambardella, Current-induced spin-orbit torques in ferromagnetic and antiferromagnetic systems, Rev. Mod. Phys. **91**, 035004 (2019).

[4] J. Ryu, S. Lee, K.-J. Lee, and B.-G. Park, Current-induced spin–orbit torques for spintronic applications, Adv. Mater. **1907148**, 1907148 (2020).

[5] M. Dyakonov and V. Perel, Current-induced spin orientation of electrons in semiconductors, Phys. Lett. A **35**, 459 (1971).

[6] J. E. Hirsch, Spin Hall Effect, Phys. Rev. Lett. **83**, 1834 (1999).

[7] E. I. Rashba, Properties of semiconductors with an extremum loop.1. cyclotron and combinational resonance in a magnetic field perpendicular to the plane of the loop, Sov. Phys. Solid State **2**, 1109 (1960).

[8] E. I. Rashba and Y. A. Bychkov, Oscillatory effects and the magnetic susceptibility of carriers in inversion layers, J. Phys. C **17**, 6039 (1984).

[9] V. M. Edelstein, Spin polarization of conduction electrons induced by electric current in two-dimensional asymmetric electron systems, Solid State Commun. **73**, 233 (1990).

[10] W. Zhang, M. B. Jungfleisch, F. Freimuth, W. Jiang, J. Sklenar, J. E. Pearson, J. B. Ketterson, Y. Mokrousov, and A. Hoffmann, All-electrical manipulation of magnetization dynamics in a ferromagnet by antiferromagnets with anisotropic spin Hall effects, Phys. Rev. B **92**, 144405 (2015).

[11] P. Zheng and D. Gall, The anisotropic size effect of the electrical resistivity of metal thin films: Tungsten, J. Appl. Phys. **122**, 135301 (2017).

[12] J. Ryu, C. O. Avci, S. Karube, M. Kohda, G. S. D. Beach, and J. Nitta, Crystal orientation dependence of spin-orbit

torques in Co/Pt bilayers, Appl. Phys. Lett. **114**, 142402 (2019).

[13] H. Wang, K.-Y. Meng, P. Zhang, J. T. Hou, J. Finley, J. Han, F. Yang, and L. Liu, Large spin-orbit torque observed in epitaxial $SrIrO_3$ thin films, Appl. Phys. Lett. **114**, 232406 (2019).

[14] Y. Du, H. Gamou, S. Takahashi, S. Karube, M. Kohda, and J. Nitta, Disentanglement of Spin-Orbit Torques in Pt/Co Bilayers with the Presence of Spin Hall Effect and Rashba-Edelstein Effect, Phys. Rev. Appl. **13**, 054014 (2020).

[15] H. Gamou, Y. Du, M. Kohda, and J. Nitta, Enhancement of spin current generation in epitaxial α-Ta/CoFeB bilayer, Phys. Rev. B **99**, 184408 (2019).

[16] H. Li, G. Wang, D. Li, P. Hu, W. Zhou, X. Ma, S. Dang, S. Kang, T. Dai, F. Yu, X. Zhou, S. Wu, and S. Li, Spin-orbit torque-induced magnetization switching in epitaxial Au/Fe_4N bilayer films, Appl. Phys. Lett. **114**, 092402 (2019).

[17] J. Ryu, M. Kohda, and J. Nitta, Observation of the D'yakonov-Perel' Spin Relaxation in Single-Crystalline Pt Thin Films, Phys. Rev. Lett. **116**, 256802 (2016).

[18] N. H. Long, P. Mavropoulos, D. S. Bauer, B. Zimmermann, Y. Mokrousov, and S. Blügel, Strong spin-orbit fields and Dyakonov-Perel spin dephasing in supported metallic films, Phys. Rev. B **94**, 180406(R) (2016).

[19] J. Sinova, S. O. Valenzuela, J. Wunderlich, C. H. Back, and T. Jungwirth, Spin Hall effects, Rev. Mod. Phys. **87**, 1213 (2015).

[20] E. M. Chudnovsky, Intrinsic spin Hall effect in noncubic crystals, Phys. Rev. B **80**, 153105 (2009).

[21] F. Freimuth, S. Blügel, and Y. Mokrousov, Anisotropic Spin Hall Effect from First Principles, Phys. Rev. Lett. **105**, 246602 (2010).

[22] V. Sih, R. C. Myers, Y. K. Kato, W. H. Lau, A. C. Gossard, and D. D. Awschalom, Spatial imaging of the spin hall effect and current-induced polarization in two-dimensional electron gases, Nat. Phys. **1**, 31 (2005).

[23] W. Zhang, W. Han, S.-H. Yang, Y. Sun, Y. Zhang, B. Yan, and S. S. P. Parkin, Giant facet-dependent spin-orbit torque and spin Hall conductivity in the triangular antiferromagnet $IrMn_3$, Sci. Adv. **2**, e1600759 (2016).

[24] T. Nan, T. J. Anderson, J. Gibbons, K. Hwang, N. Campbell, H. Zhou, Y. Q. Dong, G. Y. Kim, D. F. Shao, T. R. Paudel, N. Reynolds, X. J. Wang, N. X. Sun, E. Y. Tsymbal, S. Y. Choi, M. S. Rzchowski, Y. B. Kim, D. C. Ralph, and C. B. Eom, Anisotropic spin-orbit torque generation in epitaxial $SrIrO_3$ by symmetry design, PNAS USA **116**, 16186 (2019).

[25] C. Guillemard, S. Petit-Watelot, S. Andrieu, and J.-C. Rojas-Sánchez, Charge-spin current conversion in high quality epitaxial Fe/Pt systems: Isotropic spin Hall angle along different in-plane crystalline directions, Appl. Phys. Lett. **113**, 262404 (2018).

[26] R. Thompson, J. Ryu, Y. Du, S. Karube, M. Kohda, and J. Nitta, Current direction dependent spin Hall magnetoresistance in epitaxial Pt/Co bilayers on MgO(110), Phys. Rev. B **101**, 214415 (2020).

[27] H.-Y. Lee, S. Kim, J.-Y. Park, Y.-W. Oh, S.-Y. Park, W. Ham, Y. Kotani, T. Nakamura, M. Suzuki, T. Ono, K.-J. Lee, and B.-G. Park, Enhanced spin–orbit torque via interface engineering in Pt/CoFeB/MgO heterostructures, APL Mater. **7**, 031110 (2019).

[28] S. Woo, M. Mann, A. J. Tan, L. Caretta, and G. S. D. Beach, Enhanced spin-orbit torques in Pt/Co/Ta heterostructures, Appl. Phys. Lett. **105**, 212404 (2014).

[29] J. Kim, P. Sheng, S. Takahashi, S. Mitani, and M. Hayashi, Spin Hall Magnetoresistance in Metallic Bilayers, Phys. Rev. Lett. **116**, 097201 (2016).

[30] M. Kawaguchi, D. Towa, Y. C. Lau, S. Takahashi, and M. Hayashi, Anomalous spin Hall magnetoresistance in Pt/Co bilayers, Appl. Phys. Lett. **112**, 202405 (2018).

[31] J. Torrejon, J. Kim, J. Sinha, S. Mitani, M. Hayashi, M. Yamanouchi, and H. Ohno, Interface control of the magnetic chirality in cofeb/mgo heterostructures with heavy-metal underlayers, Nat. Commun. **5**, 4655 (2014).

[32] R. J. Elliott, Theory of the effect of spin-orbit coupling on magnetic resonance in some semiconductors, Phys. Rev. **96**, 266 (1954).

[33] Y. Yafet, Calculation of the g factor of metallic sodium, Phys. Rev. **85**, 478 (1952).

[34] E. Sagasta, Y. Omori, M. Isasa, M. Gradhand, L. E. Hueso, Y. Niimi, Y. Otani, and F. Casanova, Tuning the spin Hall effect of Pt from the moderately dirty to the superclean regime, Phys. Rev. B **94**, 060412(R) (2016).

[35] H. Nakayama, Y. Kanno, H. An, T. Tashiro, S. Haku, A. Nomura, and K. Ando, Rashba-Edelstein Magnetoresistance in Metallic Heterostructures, Phys. Rev. Lett. **117**, 116602 (2016).

[36] H. Nakayama, H. An, A. Nomura, Y. Kanno, S. Haku, Y. Kuwahara, H. Sakimura, and K. Ando, Temperature dependence of Rashba-Edelstein magnetoresistance in Bi/Ag/CoFeB trilayer structures, Appl. Phys. Lett. **110**, 222406 (2017).

[37] U. H. Pi, K. Won Kim, J. Y. Bae, S. C. Lee, Y. J. Cho, K. S. Kim, and S. Seo, Tilting of the spin orientation induced by Rashba effect in ferromagnetic metal layer, Appl. Phys. Lett. **97**, 162507 (2010).

[38] J. Kim, J. Sinha, M. Hayashi, M. Yamanouchi, S. Fukami, T. Suzuki, S. Mitani, and H. Ohno, Layer thickness dependence of the current-induced effective field vector in Ta-CoFeB-MgO, Nat. Mater. **12**, 240 (2013).

[39] A. Ghosh, K. Garello, C. O. Avci, M. Gabureac, and P. Gambardella, Interface-Enhanced Spin-Orbit Torques and Current-Induced Magnetization Switching of Pd/Co/AlOx Layers, Phys. Rev. Appl. **7**, 014004 (2017), arXiv:1701.01843.

[40] M. Hayashi, J. Kim, M. Yamanouchi, and H. Ohno, Quantitative characterization of the spin-orbit torque using harmonic Hall voltage measurements, Phys. Rev. B **89**, 144425 (2014).

[41] L. Liu, T. Moriyama, D. C. Ralph, and R. A. Buhrman, Spin-Torque Ferromagnetic Resonance Induced by the Spin Hall Effect, Phys. Rev. Lett. **106**, 036601 (2011).

[42] M. H. Nguyen, D. C. Ralph, and R. A. Buhrman, Spin Torque Study of the Spin Hall Conductivity and Spin Diffusion Length in Platinum Thin Films with Varying Resistivity, Phys. Rev. Lett. **116**, 126601 (2016).

[43] A. V. Khvalkovskiy, V. Cros, D. Apalkov, V. Nikitin, M. Krounbi, K. A. Zvezdin, A. Anane, J. Grollier, and A. Fert, Matching domain-wall configuration and spin-orbit torques

for efficient domain-wall motion, Phys. Rev. B **87**, 020402 (2013).

[44] P. M. Haney, H.-W. Lee, K.-J. Lee, A. Manchon, and M. D. Stiles, Current induced torques and interfacial spin-orbit coupling: Semiclassical modeling, Phys. Rev. B **87**, 174411 (2013).

[45] V. P. Amin and M. D. Stiles, Spin transport at interfaces with spin-orbit coupling: Formalism, Phys. Rev. B **94**, 104419 (2016).

[46] V. P. Amin and M. D. Stiles, Spin transport at interfaces with spin-orbit coupling: Phenomenology, Phys. Rev. B **94**, 104420 (2016).

[47] C. Du, H. Wang, F. Yang, and P. C. Hammel, Systematic variation of spin-orbit coupling with *d*-orbital filling: Large inverse spin Hall effect in 3d transition metals, Phys. Rev. B **90**, 140407 (2014).

[48] S.-H. C. Baek, V. P. Amin, Y.-W. Oh, G. Go, S.-J. Lee, G.-H. Lee, K.-J. Kim, M. D. Stiles, B.-G. Park, and K.-J. Lee, Spin currents and spin-orbit torques in ferromagnetic trilayers, Nat. Mater. **17**, 509 (2018).

[49] A. Manchon, H. C. Koo, J. Nitta, S. M. Frolov, and R. A. Duine, New perspectives for Rashba spin-orbit coupling, Nat. Mater. **14**, 871 (2015), arXiv:1507.02408.

[50] E. Simon, A. Szilva, B. Ujfalussy, B. Lazarovits, G. Zarand, and L. Szunyogh, Anisotropic rashba splitting of surface states from the admixture of bulk states: Relativistic *ab initio* calculations and $k \cdot p$ perturbation theory, Phys. Rev. B **81**, 235438 (2010).

[51] M. Nagano, A. Kodama, T. Shishidou, and T. Oguchi, A first-principles study on the Rashba effect in surface systems, J. Condens. Matter Phys. **21**, 064239 (2009).

[52] H. Bentmann and F. Reinert, Enhancing and reducing the Rashba-splitting at surfaces by adsorbates: Na and Xe on Bi/Cu(111), New J. Phys. **15**, 115011 (2013).

[53] Z. S. Popović, J. M. Kurdestany, and S. Satpathy, Electronic structure and anisotropic Rashba spin-orbit coupling in monolayer black phosphorus, Phys. Rev. B **92**, 035135 (2015).